MEDICAL ROBOTS

Quantifying stiffness and forces of tumor colonies and embryos using a magnetic microrobot

Erfan Mohagheghian[1]†, Junyu Luo[2]†, F. Max Yavitt[3,4]†, Fuxiang Wei[2]†, Parth Bhala[1]†, Kshitij Amar[1]†, Fazlur Rashid[1], Yuzheng Wang[5], Xingchen Liu[6], Chenyang Ji[2], Junwei Chen[2], David P. Arnold[5], Zhen Liu[6], Kristi S. Anseth[3,4]*, Ning Wang[1]*

Stiffness and forces are two fundamental quantities essential to living cells and tissues. However, it has been a challenge to quantify both 3D traction forces and stiffness (or modulus) using the same probe in vivo. Here, we describe an approach that overcomes this challenge by creating a magnetic microrobot probe with controllable functionality. Biocompatible ferromagnetic cobalt-platinum microcrosses were fabricated, and each microcross (about 30 micrometers) was trapped inside an arginine–glycine–aspartic acid–conjugated stiff poly(ethylene glycol) (PEG) round microgel (about 50 micrometers) using a microfluidic device. The stiff magnetic microrobot was seeded inside a cell colony and acted as a stiffness probe by rigidly rotating in response to an oscillatory magnetic field. Then, brief episodes of ultraviolet light exposure were applied to dynamically photodegrade and soften the fluorescent nanoparticle–embedded PEG microgel, whose deformation and 3D traction forces were quantified. Using the microrobot probe, we show that malignant tumor–repopulating cell colonies altered their modulus but not traction forces in response to different 3D substrate elasticities. Stiffness and 3D traction forces were measured, and both normal and shear traction force oscillations were observed in zebrafish embryos from blastula to gastrula. Mouse embryos generated larger tensile and compressive traction force oscillations than shear traction force oscillations during blastocyst. The microrobot probe with controllable functionality via magnetic fields could potentially be useful for studying the mechanoregulation of cells, tissues, and embryos.

INTRODUCTION

Increasing evidence demonstrates that cell-generated contractile forces (traction forces) as well as cell and/or tissue stiffness are two mechanical parameters fundamental to the functions of living cells and tissues in physiology, development, and diseases, such as cancer, cardiovascular disease, and fibrosis (*1*). Cell stiffness, the resistance to cell deformation, is known to be proportional to and depend on myosin II–mediated traction forces (interfacial forces) in single living tissue cells (*2*, *3*). However, a recent report found that actomyosin-dependent traction forces dominate architectures in monolayer epithelia, whereas tissue stiffness dominates multilayer epithelia architectures in mouse embryos (*4*), suggesting that these two quantities play different roles in embryonic development. Yet it has been challenging to quantify both three-dimensional (3D) traction force and stiffness (or modulus, which is the ratio of stress to deformation) at the same location of a biological sample. The reason for the difficulty is that to quantify traction forces, the probe must be soft and flexible so that deformation (strain) of the probe can be used to calculate the traction force if the probe's intrinsic stiffness (or modulus) is known. On the other hand, to quantify stiffness, the probe must be stiff enough that the probe can apply an exogenous force (a stress or a torque) to deform the biological sample, and hence, the stiffness can be calculated from the measured strain of the sample. Because it requires the probe to be both soft and rigid to measure these two independent mechanical quantities, it is technically challenging.

Over the past 60 years, various types of probes have been developed to quantify cell stiffness in culture. The micropipette aspiration technique (*5*) and the optical stretcher (*6*) to measure the stiffness of suspended cells have been developed. Methods have also been developed to quantify adherent cells' mechanical properties. These methods include particle tracking microrheology (*7*, *8*), laser tweezers to trap a particle on the cell surface (*9*), and atomic force microscopy (AFM) to use a cantilever to indent a cell on its surface (*10*). Other methods include magnetic twisting cytometry (MTC) that uses ligand-coated magnetic beads to stress the cell surface via integrin receptors or other specific receptors with a torque load (*11*, *12*) and a magnetic gradient pulling device (*13*). MTC has been substantially improved in recent years such that a 3D MTC can apply local stresses in any controlled direction (*14*) and can be integrated with confocal microscopy and stimulated emission detection nanoscopy to quantify cell surface complex stress or surface shear stress–induced chromatin deformation (*15*, *16*). A comparison of various methods to measure cell stiffness in the same cell type showed that different methods probe various components of the mechanical properties of the cells, but AFM and MTC measure similar values of cell stiffness (*17*). However, only a limited number of approaches can be used to quantify stiffness ex vivo or in vivo. Spatiotemporal viscoelastic properties of a

[1]Department of Mechanical Science and Engineering, Grainger College of Engineering, University of Illinois at Urbana-Champaign, Urbana, IL 61801, USA. [2]Key Laboratory of Molecular Biophysics of the Ministry of Education, Laboratory for Cellular Biomechanics and Regenerative Medicine, College of Life Science and Technology, Huazhong University of Science and Technology, Wuhan, Hubei 430074, China. [3]Department of Chemical and Biological Engineering, University of Colorado, Boulder, CO 80303, USA. [4]BioFrontiers Institute, University of Colorado, Boulder, CO 80303, USA. [5]Department of Electrical and Computer Engineering, University of Florida, Gainesville, FL 32611, USA. [6]Institute of Neuroscience, Key Laboratory of Primate Neurobiology, CAS Center for Excellence in Brain Science and Intelligence Technology, Chinese Academy of Sciences, Shanghai 200031, China.
*Corresponding author. Email: nwangrw@illinois.edu (N.W.); kristi.anseth@colorado.edu (K.S.A.)
†These authors contributed equally to this work.

zebrafish embryo have been quantified by injecting oil droplets loaded with magnetic nanoparticles, with data suggesting that the posterior elongating region has lower stiffness and more viscosity than the anterior region (*18*). Furthermore, a stiffness gradient was observed in the developing *Xenopus* brain using AFM (*19*).

Various methods of measuring traction forces on 2D (*20*–*26*) and 3D substrates (*27*–*32*) have been developed. Single-cell traction force mapping has also been extended to monolayer stress microscopy in collective cell migration (*33*, *34*). A high-resolution cell mechanical imaging platform was developed to estimate intracellular contractile forces (*35*). However, few methods are able to measure traction forces ex vivo or in vivo. For example, force was quantified using a gel-based force sensor in an isolated *Xenopus laevis* embryonic tissue (*36*). Using an oil-droplet force sensor microinjected into living tissues, anisotropic forces were quantified in living dissected mouse mandibles (*37*), and supracellular stresses were found to decrease from anterior to posterior regions and guide solid- to fluid-like transition in zebrafish embryos (*38*). Polyacrylamide (PA) bead force sensors were developed to measure forces in developing zebrafish embryos (*39*). Using ultrasound for deep tissue penetration, quantifications of solid stress in excised or in situ tumors have been achieved but with limited spatial resolution (*40*). Similarly, magnetic resonance elastography and ultrasound elastography have been applied to quantify tissue stiffness in patients with liver fibrosis or breast tumors, but the spatial resolution of these techniques is in the range of millimeters to centimeters (*41*–*43*). We have published a different approach of using an elastic microgel that can quantify isotropic and anisotropic surface stresses and has been used to quantify forces in developing zebrafish embryos in vivo (*44*). The results revealed spatial and temporal traction force variations (with a spatial resolution of 1 to 2 μm) inside the embryo from 3 to 10 hours after fertilization (*44*), suggesting that these traction forces and their spatial variations might be important in the patterning and morphogenesis of zebrafish embryos.

In this study, we present an approach by which both traction force and stiffness can be quantified at the same location of a tumor cell colony embedded in 3D matrices and in a developing vertebrate embryo using a microrobot probe controlled remotely by magnetic fields. We demonstrate that shear modulus of stem cell–like tumor repopulating cell colonies varies with 3D substrate elasticity, but their 3D traction forces do not. Moreover, traction force oscillations are observed in zebrafish embryos from blastula to gastrula. We also demonstrate that mouse embryos exhibit substantial oscillations in tensile and compressive traction forces during early to late stages of blastocyst development.

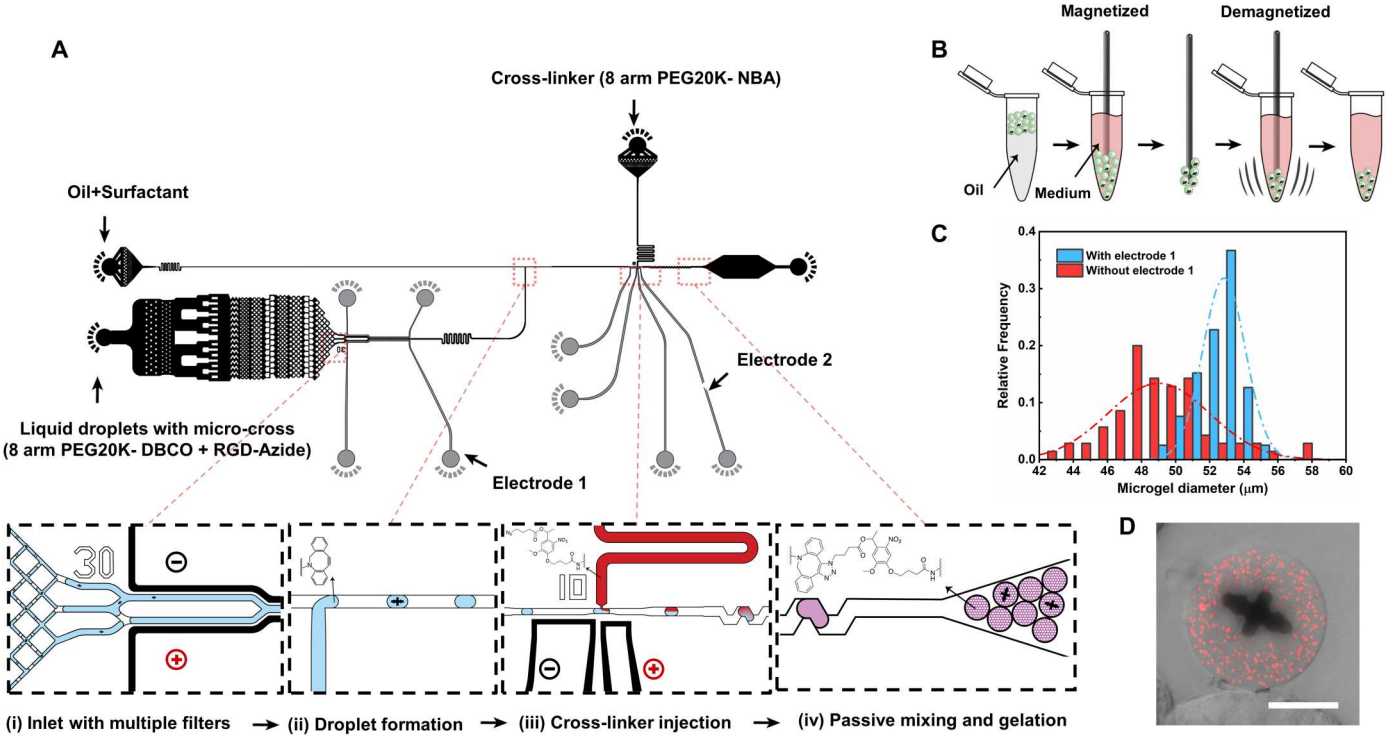

Fig. 1. Fabrication of the magnetic microrobot probe. (**A**) Computer-aided design layout of microfluidic device illustrating its working mechanism and different modules, including the inlets, T junction, picoinjection, mixing, and outlet. Polydisperse droplets of 8-arm PEG20K-DBCO (blue) with an embedded microcross are passed through multiple filters at the inlet and merged by the applied AC electric field at electrode 1 (i). PEG-DBCO droplets are formed at the T junction (ii) and moved down to the picoinjection module, where the 8-arm PEG 8-NBA (red) is injected to the passing droplets by the applied AC electric field at electrode 2 (iii). After injection, passing the droplet through the serpentine channel enhances the mixing to form a homogenous microgel containing one microcross (iv). (**B**) Schematic showing steps to resuspend the microgels from oil to cell culture medium and isolate the microrobot probe (a microgel with an embedded microcross) from the rest of the microgels using a magnetized Allen wrench (and subsequent demagnetization). (**C**) Effect of applied field at electrode 1 on size distribution of the collected microgels. (**D**) Confocal section of the microrobot probe with embedded 500-nm red fluorescent nanoparticles and biocompatible ferromagnetic microcross used to measure stiffness and traction force. Scale bar, 25 μm.

RESULTS

Fabrication and characterization of the magnetic microrobot probe

We recently developed a method of using a soft elastic round microgel to quantify 3D traction forces in a 3D cell colony or a living zebrafish embryo (*44*). To quantify stiffness or modulus of the biological sample (cancer cell colony or an embryo), we applied shear stresses, measured sample deformation, and calculated stiffness (stiffness was the ratio of stress to deformation). To achieve this goal, we first microfabricated a multilayered ferromagnetic cobalt-platinum (Co-Pt) alloy microcross using a layer-by-layer electrodeposition strategy (fig. S1A). This microcross was uniform with the following dimensions: thickness was 10.62 ± 1.64 μm (means ± SD), lengths were 30.86 ± 2.86 μm (long arm) and 21.01 ± 2.15 μm (short arm), and volume was 5116.09 ± 2041.54 μm^3 (figs. S1, B and C, and S2). The applied torque was proportional to the microcross volume, and thus, it varied by 39.9% for microcrosses from different locations on the wafer. However, the variability of the applied torque had no effect on the measured modulus because the stress-strain relationship was linear in the range of the applied stress, and thus, the modulus was independent of the stress magnitudes. The magnetic moment of the microcross varied with the external magnetic field with hysteresis (fig. S1D), suggesting that the microcross is ferromagnetic and suitable for microrobot actuation.

Next, we used a microfluidic device to embed the microcross inside a poly(ethylene glycol) (PEG) microgel (Fig. 1A). An azide-functionalized adhesive peptide, RGD (Arg-Gly-Asp) azide, and an eight-arm PEG macromer functionalized with dibenzylcyclooctyne (8-arm PEG20K-DBCO; blue) were first prepared to conjugate RGD to the PEG macromer through a strain-promoted azide-alkyne cycloaddition. This mixture was then injected as polydisperse droplets (blue in Fig. 1Ai), passed through multiple filters at the inlet, and merged by the applied AC electric field at electrode 1 (Fig. 1Ai) to assemble the microcross inside the PEG polymer. Then, the PEG20K-DBCO droplets were formed at the T junction (Fig. 1Aii) and transported to the picoinjection module, where the eight-arm PEG-nitrobenzyl azide (PEG 8-NBA) (fig. S3) was injected into the passing droplets by the applied AC electric field at electrode 2 (Fig. 1Aiii). After injection, the mixing was enhanced by passing the droplet through the serpentine channel to form a homogenous cross-linked microgel containing a magnetic microcross (Fig. 1Aiv). The microgels (each with a magnetic microcross) were gently removed using a weakly magnetizable steel wrench (Allen wrench) that was subsequently demagnetized to release the microcross-containing microgels into a test tube. This allowed us to resuspend them from oil to cell culture medium and separate them from the microgels that did not contain microcrosses (Fig. 1B). In the absence of the electrode 1, the microgels, with or without microcrosses, were polydisperse (Fig. 1C), and with the electrode 1, the size range of the probes was much narrower, with a diameter of 49.78 ± 0.91 μm (means ± SD) (Fig. 1, C and D). Next, we magnetized the microrobot probes in a 2.9-T constant magnetic field of an MRI (magnetic resonance imaging) machine (Fig. 2Ai). Then, we exposed the probes in the 3D fibrin gels of homogenous polymers to sinusoidal magnetic twisting fields in the *x*-*y* plane (0 to 25 G) (Fig. 2Aii) that were too weak to remagnetize the magnetic microcrosses but generated torques on the microrobot probe via the ferromagnetic microcross. To use the microrobot as a probe for stiffness measurement, we initially polymerized the PEG to be very stiff, with a modulus of ~10 kPa (*45*), and so, when the external magnetic field was applied, the whole microgel rotated with the microcross as a rigid body rotation without any slippage or deformation (Fig. 2Aiii). After the stiffness measurement, the microrobot probe was substantially softened by several brief episodes (5 to 10 s) of ultraviolet (UV) light exposure (50 mW/cm^2) via the radical-mediated mechanism of cleavage of the nitrobenzyl ether moiety integrated into the cross-links (fig. S4) (*45*); the magnetic field was turned off, and the probe was deformed by traction forces generated by the nearby cells/tissues and thus acted as a force sensor (Fig. 2Aiv). The effects of the microrobot probe size on UV exposure are shown in Fig. 2B. The swelling of the probe (Fig. 2C and fig. S5), as the PEG gel was depolymerized by UV light, was attributed to the binding of the water molecules to the dissociated PEG molecules. There were no effects on cell viability when the cells were exposed to UV light of 50 mW/cm^2 for up to 5 min (fig. S6), much longer than the exposure duration (<45 s), to soften the microgels in living tumor cell colonies, consistent with the published observation that exposing human mesenchymal stem cells to a comparable UV energy does not affect cell viability and traction forces (*46*). To determine the bulk modulus of the swollen microrobot probe after UV irradiation, we added dextran (2 MDa; MilliporeSigma) at various concentrations to the medium containing the probes and measured the corresponding compressive bulk strains as a function of the dextran osmotic pressure (Fig. 2D) (*47*). Using a Poisson ratio of 0.44 for PEG gels (*48*), we computed the Young′s moduli of the probes from their bulk moduli as a function of the softened microgel probes′ final diameters (Fig. 2E). The microrobot probe modulus calibration was used later for computing 3D traction forces in 3D culture. To convert the applied magnetic field strength in gauss to the shear stress onto the probe, we embedded a microrobot probe in a homogenous elastic PEG gel of 115-Pa elastic modulus (Fig. 2F, top, and fig. S7) and quantified the angular rotations of the probes, which exhibited zero-phase lag and linear rotational effects to applied sinusoidal magnetic fields [Fig. 2, F (bottom) and G]. From the calibrations in the PEG gel, we determined that the shear stress of the microrobot probe was 0.126 Pa/G of magnetic field.

Quantifying cancer cell colony modulus by the microrobot probe

We used the probe to quantify cell colony modulus in 3D cultures. Using a previously published method (*49*), we first selected and grew single malignant tumor-repopulating cells (TRCs) from a general population of the mouse melanoma B16-F1 cell line into cell colonies in a soft (90-Pa) fibrin gel for 3 days (Fig. 3A). Subsequently, the tumor cell colonies were gently removed, mixed with the RGD-conjugated PEG microrobot probes, and cultured on rigid glass dishes covered with 400-Pa fibrin gel (to mimic heterogeneous substrate stiffness) (Fig. 3B, top left). Alternatively, the mixture of cancer cell colony probe was plated on 1-kPa PA gel–coated glass [the PA gel was about 70 μm in thickness, so there was no rigid glass (around 1 GPa) effect], and the mixture was covered with 1-kPa fibrin gel (to mimic uniform 3D substrate stiffness) for three additional days (Fig. 3B, bottom left and right). The tumor cell colonies exhibited more spread morphologies (fig. S8) and grew more rapidly in the 400-Pa fibrin gels (Fig. 3B, top

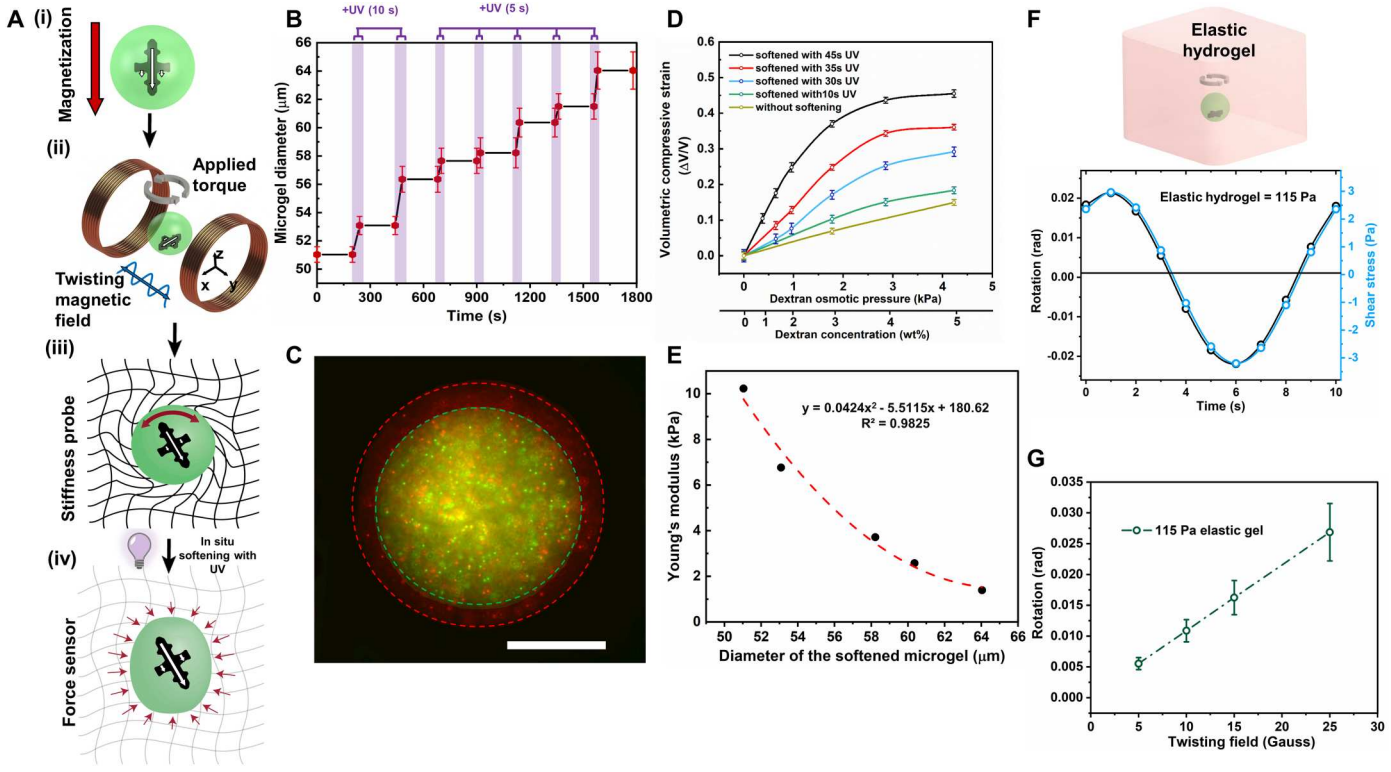

Fig. 2. The magnetic microrobot as a stiffness probe and a force sensor. (**A**) Schematic showing steps of using the microrobot to measure stiffness and 3D traction forces. The microrobot is permanently magnetized along the *x* axis (white arrow) in a 2.9-T MRI machine (red arrow) (i), followed by a sinusoidal twisting field along the *y* axis, resulting in the oscillating magnetic torque in the *z* direction (ii). The applied torque (red arrow) deforms the microenvironment for stiffness measurements (iii), and then the microrobot probe is softened by 405-nm UV to measure the 3D traction forces exerted onto the probe (iv). (**B**) UV degradation (fig. S3) and swelling evolution of the microgels with respect to the stepwise UV irradiation (exposure times not to scale) shows the stable size of the microgel after each softening exposure (10 or 5 s) with UV irradiation (50 mW/cm^2). For each time point of gel measurement after UV degradation, means ± SD, n = 15 microgels. (**C**) Representative fluorescent image of the microgel after UV irradiation shows partial degradation and microgel swelling with wider distribution of fluorescent particles (green dashed line, before UV; red dashed line, after UV). Scale bar, 25 μm. (**D**) Volumetric compressive strains of the UV-degraded microrobot probes in response to hypertonic osmotic pressure (as a result of dextran addition). The microrobot probes were first softened with different UV irradiations (45, 35, 30, or 10 s) and allowed to swell to their final diameter. Subsequently, dextran with different concentrations was added to compress the UV-degraded microrobot probes. Means ± SEM, n = 20 microgels per UV irradiation condition. (**E**) Relationship between Young's modulus of the softened microrobot probe with respect to its diameter, converted from bulk modulus that was calculated from the linear fit on the first three data points of the curves in (D), using a Poisson ratio of 0.44 for PEG hydrogels. (**F**) Schematic showing the calibration of the microrobot probe embedded inside the PEG elastic hydrogel (top); the applied sinusoidal magnetic field was 25 G at 0.1 Hz, the peak applied shear stress was 3.15 Pa, and the corresponding rotation did not exhibit any phase lags (bottom). (**G**) The relationship between the applied twisting field and the microrobot probe rotation was linear, showing that the probe generated 0.126 Pa/G. For each applied twisting field, means ± SEM, n = 7 microrobots.

right) than in the 1-kPa fibrin gels (Fig. 3B, bottom right), which is consistent with a published report that TRCs grow very slowly and enter dormancy in 1-kPa fibrin gels by expressing COUP transcription factor 1 and inhibiting Ki67 (*50*). The distance between microrobot midplane and top surface of 1-kPa PA gel was 48.06 ± 5.26 μm (means ±SEM), and there was little probe rotation–induced PA gel deformation (fig. S9). As expected, the colony exhibited viscoelastic behaviors, with phase lags in response to the shear stress from the microrobot probe's in-plane rotation as a result of a sinusoidal magnetic field at 0.1 Hz (Fig. 3C). The tumor cell colonies exhibited more angular rotations in 1-kPa PA gel +1-kPa fibrin gel than in rigid glass +400-Pa fibrin gel (Fig. 3D), but the phase lags were similar under both conditions and were independent of the applied stress (Fig. 3E). From these stress-strain relationships, complex shear modulus, storage shear modulus, and loss shear modulus were computed (fig. S10). Disrupting F-actin with latrunculin A increased rotation of the probe, and polymerizing F-actin with jasplakinolide decreased rotation of the probe (fig. S11), consistent with the published observation that actomyosin bundles from the cells surrounding the microgel are the primary contributor to the measured traction forces and extending published findings in stiffness in single cancer cells and normal cells.

Quantification of modulus and 3D traction forces in a cancer cell colony

After the colony stiffness measurement, we used UV light to degrade and soften the PEG gel of the microrobot probe, quantified the deformation of the probe induced by the surrounding cells (Fig. 4A), and treated the cells with Tween 20, which had no effects on microgel diameter (fig. S12) that killed the cells to obtain stress-free conditions (Fig. 4B). Displacements, normal traction force, shear traction force, and total traction force were measured in a TRC colony, showing that the traction forces were dominated by compressive traction forces (Fig. 4C). Although

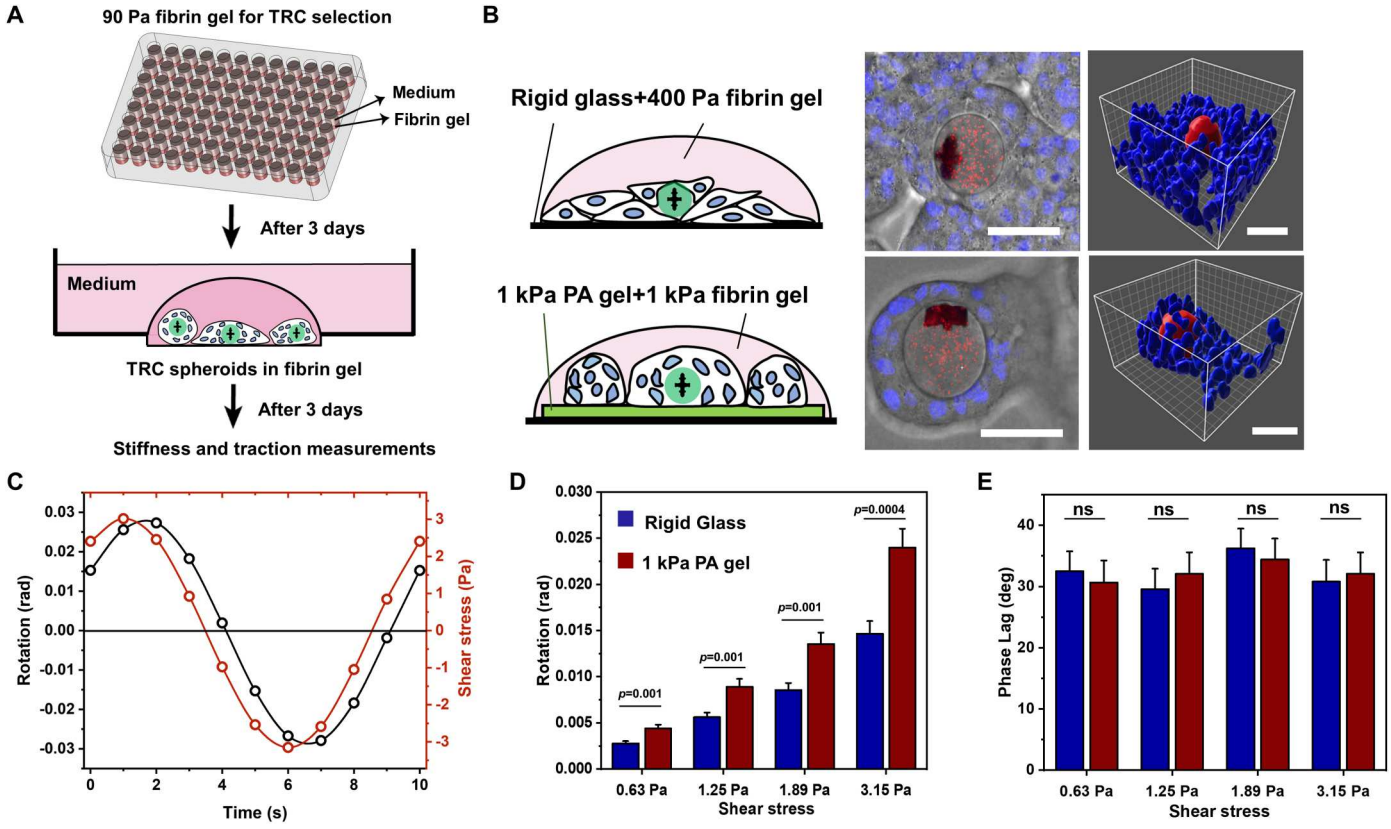

Fig. 3. The microrobot probe quantifies stress-strain relationship of a cancer cell colony in a 3D substrate. (**A**) Schematic of preparation of cells for stiffness and force measurements. (**B**) TRCs plated on rigid glass or 1-kPa PA gel and embedded in 400-Pa or 1-kPa fibrin gels, exhibiting distinct nuclear morphologies (blue, stained with Hoechst 33342 nuclear stain) around the microrobot probe (red). The top and bottom images on the right side correspond to schematics of rigid glass and 1-kPa gels on the left. Scale bars, 50 μm. (**C**) An example of quantified angular rotation of a microrobot probe in response to applied shear stress for a single colony on a 1-kPa PA gel at 25 G and 0.1 Hz. (**D**) Stress-strain relationship of cancer cell colonies at 0.1 Hz; greater strains (rad, radians) indicate softer cell colonies on 1-kPa PA gels. Note that because of variations in microcross size, there were 39.9% errors (SD) in actual values of applied shear stress. (**E**) Associated phase lags [degrees (deg)] do not vary with applied stress or with substrate stiffness. For (D) and (E), means + SEM; $n = 31$ microrobot probes for 0.63, 1.25, and 1.89 Pa on rigid glass; $n = 30$ probes for 3.15 Pa on rigid glass; $n = 28$ probes on 1-kPa PA gel for 0.63, 1.89, and 3.15 Pa; $n = 27$ probes for 1.25 Pa; three independent experiments for rigid glass condition; four independent experiments for 1-kPa PA gel condition; ns, not statistically different. Two-tailed Student's *t* test was used.

there were differences in probe rotations between the cells plated on 1-kPa PA gel and those on rigid glass (Fig. 4D; also see Fig. 3D and fig. S10), the mean traction forces (normal or shear) were similar (Fig. 4E), suggesting that for these malignant tumor cell colonies in 3D, stiffness changes do not follow traction force changes. This is in contrast to published observations in noncancerous single tissue cells (*3*).

Quantifying stiffness and traction forces in zebrafish embryos

Next, microrobot probes were injected into zebrafish embryos, and stiffness and traction forces were quantified (Fig. 5, A to J, and fig. S13) using a similar protocol as that for the above tumor cell colony. Zebrafish embryos exhibited viscoelastic responses to the applied shear stress (Fig. 5, B and G, and fig. S13), and complex modulus, storage modulus, and loss modulus were computed; the complex modulus was dominated by the storage modulus because the loss modulus was lower (Fig. 5K). The embryos exhibited both normal (tensile and compressive) and shear traction force oscillations (Fig. 5, L and M). Taking a closer look, we found that there existed two (large and small) distinct sets of traction force oscillation amplitudes (Fig. 5N). The large traction force oscillation amplitudes were associated with the microgel probes that were located at the embryos (four probes in three embryos); the small traction force oscillation amplitudes were associated with the microgel probes that were located at the embryo-yolk boundaries (eight probes at the embryo-yolk boundaries or in the yolk cell) (figs. S14 to S16). These results suggest that different cells at various locations in the embryo generate different amplitudes of normal and shear traction force oscillations. The data of small normal oscillations in normal traction forces are in the same range as those published previously (*18*, *37*–*39*). However, in those previous studies, no shear traction forces or large normal traction force oscillations were reported. Our results suggest that normal traction forces, shear traction forces, and local moduli might help drive development and shape changes of early zebrafish embryos.

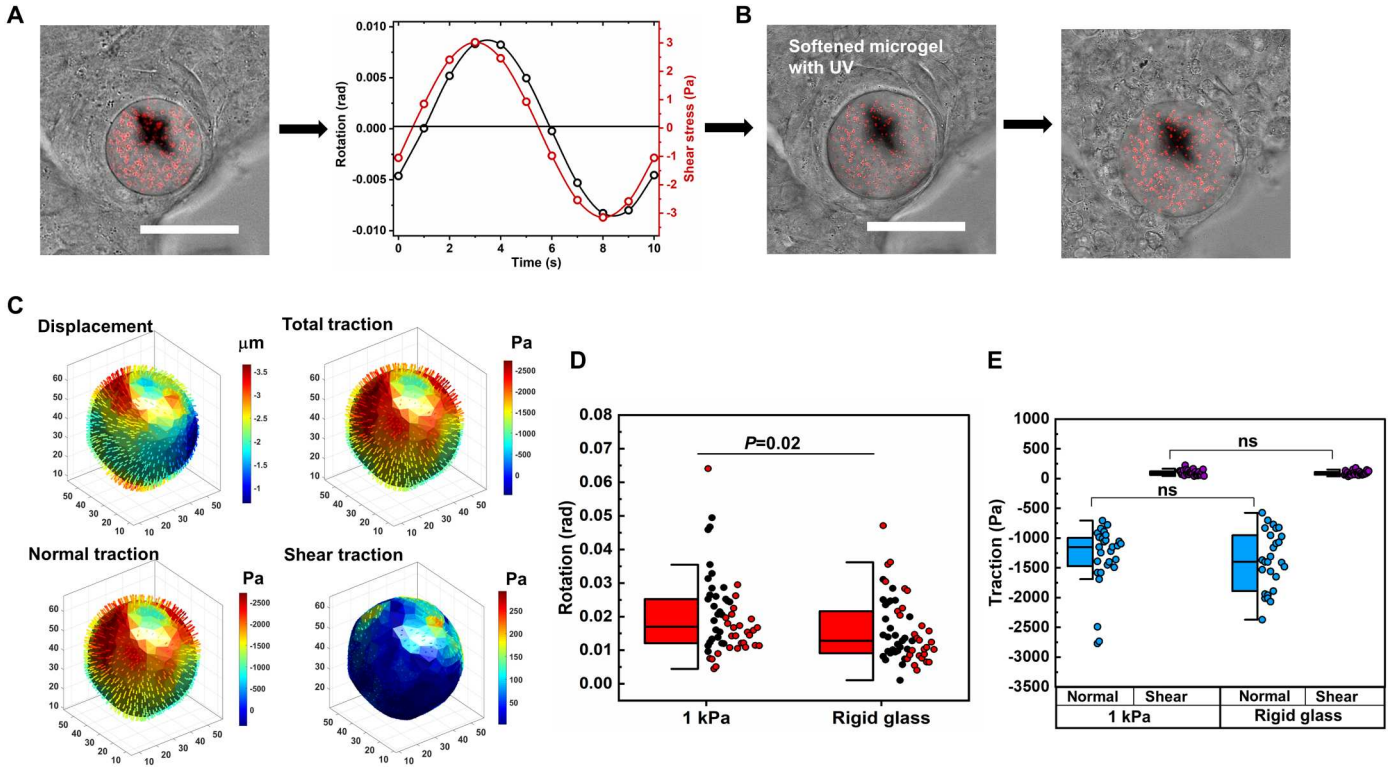

Fig. 4. Quantification of modulus and traction forces in a cancer cell colony using the microrobot probe. (**A**) An example of the microrobot probe encapsulated inside the 3D TRCs on rigid glass covered with 400-Pa fibrin gels (left); measured angular rotation of the probe in response to a sinusoidal magnetic twisting field at 0.1 Hz (right). Scale bar, 50 μm. (**B**) The microrobot probe was then softened by 405-nm UV irradiation for 30 s (left) to obtain its 3D deformation field (note the surface deformation of the probe), followed by treating the cell colony with Tween 20 to get stress-free conditions for traction force calculation (right). Scale bar, 50 μm (applies to both images). (**C**) 3D deformation and traction force maps of the corresponding microrobot probe. (**D**) For angular rotation (rad, radians): Red dots denote tracked probes for which corresponding normal and shear traction forces are shown; black dots are partial data from rotations of the probes in Fig. 3D. All strains are measured in response to 3.15-Pa stress at 0.1 Hz. Corresponding calculated complex shear modulus for 1-kPa and rigid glass are 203.3 ± 16.4 and 315.6 ± 51.5 Pa, respectively; means ± SEM; $n = 58$ probes on rigid glass; $n = 56$ probes on 1-kPa PA gel. (**E**) Summarized average normal and shear traction forces with corresponding angular rotations (inversely proportional to modulus) of microrobot probes embedded in TRC colonies on 1-kPa PA gel +1-kPa fibrin gels or on rigid glass +400-Pa fibrin gels. Solid lines in the box plots correspond to 25th percentile, median, and 75th percentile; $n = 27$ probes on rigid glass; $n = 28$ probes on 1-kPa PA gel for traction force data; three independent experiments. Two-tailed Student's *t* test was used.

Mouse embryos exhibit large tension and compression oscillations

We further explored whether it was possible to quantify forces in a developing mouse embryo. Because the mouse embryos are too small (<100 μm in diameter) to be injected with the microgel with the magnetic cross (~50 μm in diameter), we injected a small-sized RGD-alginate soft (Young's modulus = 3.1 kPa; Poisson ratio = 0.4) elastic round microgel (25 μm in diameter) without the magnetic cross (*44*) into a mouse embryo. Microgels were injected at the 16-cell stage (morula) [embryonic day 3.0 (E3.0)] into mouse embryos, and substantial deformations of multiple microgels in several embryos were observed at E4.0 (fig. S17). An individual microgel in an embryo was tracked such that normal traction forces and shear traction forces were mapped from the time of injection (0 hour) to 27 hours later (fig. S18, A and B). The traction forces were dominated by normal traction forces because the magnitudes of shear traction forces were much smaller; large oscillatory normal (tensile and compressive) traction forces were observed, suggesting that the embryo was generating pulling and pushing forces during the blastocyst stage (fig. S18C). Another microgel at similar *x*-*y* positions in the same embryo but at a different *z* height (around 25 μm below) exhibited similar traction force oscillations, except that the magnitudes and the direction of normal traction forces from 7 to 9 hours were different (fig. S19). The embryo pushed and squeezed the two microgels out between 27 and 31 hours after microgel injection (movies S1 to S3), suggesting the protective response from this embryo to extrude the inert and biocompatible microgels, reminiscent of the observation of aneuploid cell removal in human embryos and gastruloids (*51*). Similar large traction force oscillations were observed in three other embryos, and the amplitudes of normal traction forces (~1000 Pa) were much greater than those of shear traction forces (~100 Pa) (fig. S18F), distinct from what was observed in zebrafish embryos. These results suggest that cell-generated traction forces are important in regulating early embryogenic development and that different species of vertebrate might use different types of forces (normal versus shear) to drive embryogenesis.

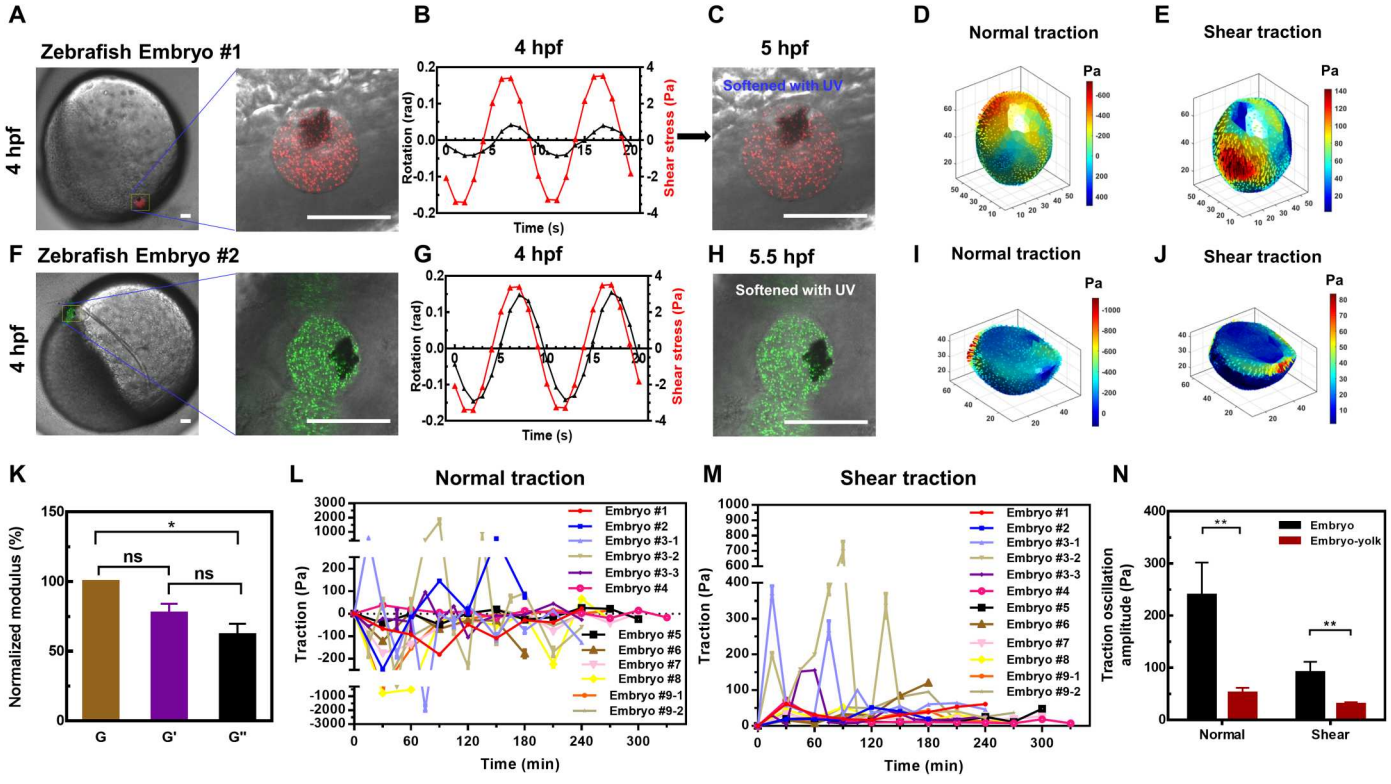

Fig. 5. Quantification of modulus and traction forces in a zebrafish embryo by the microrobot probe. (**A** to **E**) Experimental results of zebrafish embryo #1. (A) An microrobot probe was injected into an embryo at ~3.0 hpf (hour post fertilization) and imaged at 4.0 hpf (left, low magnification; right, high magnification). Scale bars, 50 μm. (B) A sinusoidal magnetic field (red) was applied at 3.5 Pa at 0.1 Hz, and the resulting probe angular rotation (black) was quantified. The phase lag between input signal and output signal was 30°. (C) Brief UV light (5 mW/cm^2) was exposed for 6 min to photodegrade and soften the PEG microgel to the final diameter of 60 μm and Young's modulus of 2.5 kPa. (D and E) Normal and shear traction forces exerted onto the probe by the surrounding cells. (**F** to **J**) Experimental results of zebrafish embryo #2. Note that yellow-green fluorescent nanoparticles were embedded into this microrobot probe for traction force quantification and that there is another probe near this probe at a different height. Scale bars, 50 μm. The phase lag between input signal and output signal was 50°. (**K**) Normalized moduli (complex modulus G, storage modulus G′, and loss modulus G″) from the original data in (B) and (G) and fig. S13, using the phase lags of 30°, 50°, and 36° and the probe-tissue contact area (which was 20% for embryo #1, 60% for embryo #2, and 10% for embryo #10) to adjust to the final effective applied shear stress. The average complex modulus G is 242 ± 62.7 Pa. Means ± SEM; $n = 3$ embryos; three separate experiments. $P = 0.0394$ between G and G″; $P = 0.0768$ between G and G′; and $P = 0.2092$ between G′ and G″. *$P < 0.05$; ns, not significantly different. (**L** and **M**) Average normal traction forces (L) and shear traction forces (M) as a function of development from blastula to gastrula. (**N**) Amplitudes of normal and shear traction force oscillations in zebrafish embryos. The traction forces were subdivided into two groups depending on the position of microgels. Traction forces in each group at different time points were averaged. Note that absolute amplitudes (but not directions, tensile or compressive) are averaged. Means ± SEM; $n = 43$ oscillations from four embryos for the embryo group; $n = 77$ oscillations from eight embryos from embryo-yolk group, respectively. $P = 0.0046$ between embryo and embryo-yolk for normal tractions; $P = 0.0054$ for shear tractions. **$P < 0.01$; two tailed Student's t test was used.

DISCUSSION

In this study, we report the development of a microrobot probe that was used to quantify 3D traction forces and stiffness at the same location of a cell colony in 3D culture and a developing vertebrate embryo. We show that the modulus of malignant tumor–repopulating cell colonies varies with 3D substrate elasticity, but their 3D traction forces do not. This conclusion is further supported by the observation that there is no correlation between traction force and modulus in tumor cell colonies when local modulus and traction force at the same site in each colony are analyzed (fig. S20). This finding is in accord with the observation that skin tumor stem cell invasion in multiepithelia architecture in mouse embryos in vivo depends on local tissue stiffness heterogeneity but not on cellular forces (*4*). Both zebrafish and mouse embryos generate substantial traction force oscillations during early embryonic development, but in zebrafish, normal and shear traction force oscillations were comparable in amplitude, whereas in mouse embryos, normal traction force oscillations dominate over shear traction forces.

A method of injecting oil droplets loaded with magnetic nanoparticles was used to quantify the stiffness of zebrafish embryos in a previous study (*18*). However, this magnetic nanoparticle–filled oil droplet approach used eight permanent magnets; in addition, the application of an on-or-off step function force depends on the movement of the magnets to exert magnetic fields to the nanomagnetic particles, and hence, no dynamic properties of biological samples can be measured. In contrast, our microrobot probe can be used to apply dynamic mechanical loading of physiological frequencies (0.1 Hz, comparable to the human resting breathing frequency of about 0.2 Hz) and amplitudes (0.6 to 3.5 Pa, covering the range of about 1.5-Pa shear stress due to fluid shear flow in blood vessels). Rheological properties, such as storage modulus

and loss modulus, of living samples in the range of 10 to 500 Pa (considering the limit in rigid body rotation assumption for the probe of 10 kPa; for the higher biological sample modulus of 5 kPa, the probe modulus needs to be increased to 100 kPa) can be quantified. In addition, because of the intrinsic incompressibility of the oil droplet (*38*, *39*), no isotropic tensile or compressive traction forces or shear traction forces can be measured. In contrast, 3D isotropic or anisotropic normal or shear traction forces in the range of 10 to 3000 Pa at the same local site of a biological sample can be quantified using the microrobot probe. Because the microrobot probe can be dynamically softened by varying the duration of the UV exposure to tune its modulus, our current probe was capable of quantifying a wide range of 3D normal and shear traction forces generated by a biological sample or tissue. This has not been achieved by the oil droplet method (*37*, *38*) or the PA bead force sensor methods (*39*, *52*), which can only measure normal traction forces.

One technical issue is whether the presence of the magnetic microcross within the elastic PEG microgel alters the measured traction forces. We explored this possibility and found that the presence of the magnetic cross inside the microgel gel had little effect on the traction forces (fig. S21). Furthermore, after the microgels were swollen and softened by UV light, the normal and shear traction forces did not vary with the microgel diameter (fig. S21). These findings suggest that brief exposures to UV light in TRCs in a colony to a different local substrate stiffness do not alter the cells′ traction forces, suggesting the existence of mechanical memory in these cells, consistent with a previous finding of mechanical memory in stem cell fate (*53*). Another technical issue is whether the position and orientation of the ferromagnetic microcross inside the microgel relative to the magnetizing field affects the torque generation. Comparing the microgel containing the microcross at the center with the microgel containing the microcross at an offset position, we found that both microgels and in-plane and out-of-plane microcrosses generated similar angular rotations and maximum centroid displacements (fig. S22). This suggests that the effects of microcross offset–generated pivoting on probe rotations were negligible and that the orientation of the microcrosses did not influence modulus measurements. When exposing sensors to UV light to soften them, the light might travel through the surrounding tissue and degrade the polymer, but it is possible that the metallic microcrosses could present a barrier to light penetration and soften the gel in a nonhomogeneous manner, yielding stiffness variability across the surface of the sensors and thus resulting in underreporting of traction force stresses on the nondegraded side of the microgels. To specifically investigate this possibility, we exposed a microgel containing the microcross to UV light and quantified the change in area at 5 μm above and below the microcross. The rationale was that if the effect of the presence of the metallic microcross was substantial, then the area below the microcross would not change much because the PEG gel in this area would not be degraded. We found that the changes in area at both places were very similar (fig. S23), suggesting that the presence of metallic microcross did not play a notable role in preventing degradation of the PEG gel in response to UV exposure. The PEG microgel below the microcross may still be masked from the UV light, but this part of the PEG might have negligible effect on the microgel strains because the stress from the outside decreases very quickly from the microgel surface.

The data for the microrobot probes of different diameters show similar traction forces, suggesting that the short duration of UV softening (<45 s) does not alter the traction force measurements, consistent with the report that within 60 s, the traction forces exhibit negligible changes in response to substrate stiffness elevation (*25*). However, alteration of substrate stiffness for 5 to 15 min does change cellular traction forces (*25*). The average traction force of TRC colonies on 1-kPa gel or on rigid glass is 1.3 kPa, 3.5-fold higher than the published result of 400-Pa mean traction force of tumor cell colonies in 0.4-kPa fibrin gels (*44*). Part of the difference in traction forces might be due to the fact that before UV exposure, the microgel had a stiffness of 10 kPa, whereas the microgel in the previous study (*44*) had a stiffness of 1.5 kPa. This will be investigated in future work by using soft microgels to quantify traction forces and then stiffening the microgel dynamically to examine the local changes in traction forces for a given substrate stiffness. In addition, the orientation of the magnetic cross relative to the magnetization field might affect the magnetic moment of the cross in response to the external magnetic field because the dimensions of the cross were not symmetrical. We have found that the magnetic moments of the microcross were very similar for in-plane and out-of-plane magnetizations (fig. S1D), suggesting that the microcross orientation had little effect on the magnetic moment of the microcross. Because the microcross is ferromagnetic, the probe can function as a microrobot controlled by external magnetic fields, useful for remote actuation in in vivo settings.

In the current study, the PEG-based microgel was softened and swollen by UV exposure to degrade cross-links of the PEG polymer. This introduced a uniform tensile stress on the microgel sensor, which might be biased toward increased normal stresses. However, because the viscous behaviors of the surrounding cells have a delay time of less than 1 s (Fig. 3, C and E), this was too short to contribute to images of the traction quantification taken tens of seconds after UV exposure and 2 hours after Tween 20 treatment to obtain stress-free conditions. To further determine whether the presence of fibrin gels influenced the PEG microgel swelling, we measured microgel diameters in response to UV before and after degradation of the 1-kPa fibrin gel. There was no significant difference between microgel diameters before and after fibrin gel degradation (fig. S24), suggesting that the presence of the fibrin gel did not contribute to the microgel swelling as a result of UV light–mediated PEG polymer degradation. Because the stiffness of the tumor cell colony was lower than 1 kPa (fig. S10), the restrictive effect of both tumor cells and fibrin gels on microgel swelling would be less than the fibrin gel alone. All these data suggest that the uniform and static tensile swelling stress on the microgel does not contribute to the compressive and shear stresses on the microgel sensor from tumor cell colonies and dynamic force oscillations from embryos. The microrobot probe could quantify both subcellular tractions (Fig. 4C) and total traction forces from multiple cells (Fig. 4E) on the microgel. The total traction measurements were on the same length scale as the stiffness measurement, in which multiple cells contribute to the resistance to rotation of the same probe. These results suggest that the magnetic microrobot could be used to probe both stiffness and traction forces at the same location of living tissues.

Previous studies have found that cell stiffness is proportional to cell prestress and thus to cell traction forces in single living tissue cells (*3*). In addition, cell stiffness and cell prestress (traction

forces) increase with 2D substrate elasticity (*54*). In contrast, we found that mouse melanoma tumor–repopulating cell colonies in 3D culture vary their stiffness but not traction forces in response to changes in 3D substrate elasticity, distinct from previous findings in single normal cells but reminiscent of the observation of multilayer epithelia in mouse embryos (*4*). It is possible that the TRCs that were seeded directly on the substrate or very close to the substrate (<5 μm above) varied in both traction forces and moduli with substrate elasticity. However, a previous study showed that cell stiffness and traction forces on 2D substrates were not correlated in breast cancer cells but were correlated in noncancerous epithelial cells (*55*). Our current finding is consistent with this observation but extends it to melanoma tumor–repopulating cells in 3D substrates, suggesting that the noncorrelation between stiffness and traction forces might be a distinct feature of malignant tumor cells. It was reported that mammary epithelial cells on a 2D soft (<150 Pa) matrix exhibit spheroid shapes and, on a 2D stiff (>3000 Pa) matrix, exhibit spread shapes and transform into malignant tumor cells (*56*). In this study, we have generated two different 3D matrix microenvironments. Under one condition, stem cell–like tumor–repopulating cells were plated on top of rigid glass and were covered with 400-Pa fibrin gels to simulate a heterogeneous mechanical tumor microenvironment. Under another condition, the TRCs were plated on 1000-Pa PA gels and were covered with 1000-Pa fibrin gels to simulate a uniform mechanical microenvironment. The mouse melanoma tumor–repopulating cell colonies were spread and grown under the heterogeneous mechanical microenvironment condition but stayed round in the uniform mechanical microenvironment and were likely dormant, as reported recently (*50*). It appears that heterogeneous and homogeneous 3D mechanical environments have different effects on tumor cell behaviors and functions. Additional studies are needed to determine why these tumor cells alter their stiffness but not traction forces in these two different mechanical microenvironments. A recent study that used fluorescent nanoparticles to decorate the extracellular matrix and embed magnetic particles to measure local matrix mechanics found that cancer cell protrusions generated forces in the nano-Newton range during invasion (*57*). In contrast, our probe could be used to quantify traction force and modulus using the same probe at the same location of the cancer cell colony. Furthermore, we found that the modulus of zebrafish embryos was on the order of a few hundred pascal, in the same range as the stiffness measured with the oil droplet probe, where spring-dashpot models have to be introduced to extract elastic modulus or viscosity (*18*). In contrast, our microrobot probe was model independent.

Few studies have been able to quantify forces generated by developing vertebrate embryos. Although it is generally accepted that nonmuscle myosin II–mediated forces regulate embryonic development, whether the magnitude of the forces and what forces (shear or normal) are important in shaping embryonic development remain elusive. It is known that calcium signaling regulates embryonic development (*58*); however, it is not clear how calcium signaling in individual cells is manifested as oscillations of normal and shear forces of cells, which drive cell shape changes and possibly tissue pattern formation in embryos. In a previous study, internalized nanodevices were used to track intracellular forces and mechanical properties in a one-cell mouse embryo (*59*). In the present study, using the alginate-microgel and the PEG-microrobot probes, we found that zebrafish and mouse embryos generate substantial oscillations of traction forces during early stages of development, suggesting that these force oscillations might be important in driving patterning, organization, and development of the embryos. Our results of force oscillation in zebrafish are consistent with the findings of bulk periodic actomyosin oscillation waves that drive segregation of ooplasm from yolk granules in zebrafish (*60*). Shear traction forces in mouse embryos are smaller than normal traction forces and are 100 to 200 Pa in magnitude (fig. S18), lower than the 300-Pa pressure observed during hydraulic fracturing of cell-cell contacts to form a blastocoel (*61*). We have found that the compressive and tensile stresses oscillate between 1000 and 2000 Pa when the microgel probe was squeezed and pulled by the embryo before blastocyst hatching, comparable in magnitude to the value of about 1500 Pa of the maximum pressure (normal stress) of mouse blastocyst hatching using a hydrogel-based microdeformation assay in a previous study (*62*). The protective response of the mouse embryo by extruding a foreign, inert, biocompatible, and micro-sized object in this study is reminiscent of the observation of aneuploid cell depletion in mammalian embryos (*51*). The zona pellucida is necessary for successful implantation, and implantation rate is critically dependent on the physiological range of the zona pellucida shear modulus (*63*). Using a micropipette aspiration method to measure surface tension of blastomeres of mouse embryos whose zona pellucidae are dissected out, researchers have shown that different contractilities in blastomeres trigger cell sorting (*64*) and that pulsatile membrane contraction forces drive compaction (*65*). However, normal and shear traction forces in the embryos cannot be quantified with the micropipette aspiration approach. In addition, the magnitudes of surface tension obtained from the embryos devoid of zona pellucida are possibly lower than those from intact embryos because shear modulus of the zona pellucida is likely to be important in force generation in embryos. In contrast, our alginate-based elastic microgel probe could quantify normal and shear traction forces in intact mouse embryos, and large tensile and compressive traction force oscillations were observed in the mouse embryos, demonstrating its utility for mouse embryos under physiological conditions.

In conclusion, we have developed a microrobot probe that can quantify stiffness and cell traction forces in in vitro culture and in vivo. This probe could potentially be used to remotely stimulate cells, embryos, and tissues to study force-regulated cell fate and differentiation by extending the duration of force application via the in-plane or out-of-plane magnetic twisting fields. The microrobot probe may also be controlled via x, y, and z magnetic fields with different amplitudes, frequencies, and phase lags to generate spiral rotations and movements of the microprobe (*14*, *15*) to stimulate living cells in tissues and embryos and to assay for biochemical activities and biological responses. This microrobot probe could potentially be particularly useful for remote control under in vivo conditions using various modalities of the magnetic field, akin to a micrometer-sized version of a magnetically controlled telerobot (*66*). By tuning the microrobot's stiffness and size and combining the probe with recently developed approaches of embryo culturing platforms for ex utero culture of mouse embryos (*67*, *68*), it might be possible to gain insights into the role of forces and mechanics in gastrulation and organogenesis during mammalian embryonic development.

MATERIALS AND METHODS

Fabrication of biocompatible ferromagnetic microcrosses

An array of Co-Pt (cobalt-platinum) microcrosses was fabricated onto a 4-inch single-side-polished silicon wafer (Pure Wafer, San Jose, CA) following previously reported methods with some modifications (*69*). First, the seed-layer stack of titanium (Ti) adhesion layer (45 nm), TiN (titanium nitride) diffusion barrier (45 nm), titanium (Ti) adhesion layer (45 nm), and Cu (copper) conductive layer (80 nm) were sequentially sputtered (AJA ATC Orion 8 UVH, AJA International) onto the wafer as shown in fig. S1. A microcross pattern was then transferred on to the 10-μm spin-coated positive photoresist AZ9260 (Microchemicals Inc.) by exposing it to UV light (I line 365, EVG 620 Mask Aligner, EV Group) through a chrome mask designed by AutoCAD (Autodesk Inc.). The resulting wafer was treated with oxygen plasma for 3 min under 150-W power (March Jupiter III) to remove any resist residues. Before the electrodeposition, the wafer was soaked in diluted sulfuric acid [H_2SO_4 (95 to 98%), H_2O = 1:10 volume ratio] to remove any layer of copper oxide that may have formed on the wafer. The electrolyte solution was made by first heating the 0.025 M diamine-dinitrito platinum (II) solution [$Pt(NH_3)_2(NO_2)_2$] (MilliporeSigma) at 75°C for 4 hours, followed by addition of cobaltous sulfamate [$Co(NH_2)_2(SO_3)_2$] (Alfa Aesar) and ammonium citrate [$(NH_4)_2C_6H_6O_7$] (MilliporeSigma) to get the final concentration of 0.1 M for each solution. Subsequently, pH was adjusted to 7 by NaOH. Electroplating was carried out in a custom-made galvanostatic cell with 1 liter of electrolyte at room temperature without stirring, using a Pt counter electrode. A current density of 50 mA/cm^2 was applied between two electrodes for 60 min to deposit 10 to 11 μm of Co-Pt. The deposited Co-Pt was then annealed to induce phase transition from disordered A1 phase to the ordered $L1_0$ phase with high coercivity. The annealing step was performed in a tube furnace under forming gas (4% H_2 + 96% N_2) at 675°C with a ramp rate of 20°C/min and a dwell time of 30 min. Cobalt and platinum are known to be biocompatible (*70*, *71*). The biocompatible Co-Pt ferromagnetic microcrosses were then detached from the wafer by light sonication in a water bath and subsequently collected in a 15-ml centrifuge tube. Initially, two designs were considered for the ferromagnetic microstructure: cross and bar. For the bar structure, we were able to consider the filter channel width less than the junction width because the individual bar and even two bars (aggregated together) were able to align themselves to the filtration channel and pass through without clogging the junction. However, we noticed that the cross design was less prone to aggregation because of the smaller contact area between the crosses, but the cross structure tended to clog the microfluidic device much more at its T junction. Reducing the filter channel width at the inlet to the same width as in the junction resulted in the filtration of most of the crosses, shorter lifespan of the microfluidic device, and much fewer collected microrobots with crosses. On the basis of the above observation, we decided to design the microcross with one side (21 μm) smaller than the other side (31 μm) and with small protrusions to reduce the contact area between the microcrosses to optimize the processes of collection and encapsulation of the microcrosses inside the PEG gels in the microfluidics channel.

Microrobot probe generation

Microfluidic T junctions were used to manufacture photodegradable microgels using picoinjection to introduce cross-linkers in the droplets for high-throughput microdroplet manufacturing. The device contained one inlet for oil phase injection and two inlets for aqueous solutions, including the solution that forms droplets and the cross-linker solution injecting at the picoinjection channel. A total volume of 400 μl of mixture was obtained for forming the droplets by prereacting 4.5 weight % (wt %) 8-arm PEG-DBCO [molecular weight (MW) = 20 kDa] containing 2×10^4 microcrosses with 0.5 mM Cyclo-RGD-azide (Vivitide, catalog no. RGD-3749-PI) for 15 min on ice in deionized water, followed by addition of red fluorescent nanoparticles (0.5 μm in diameter, carboxylate-modified; Thermo Fisher Scientific) or yellow-green fluorescent nanoparticles (0.5 μm in diameter, nonfunctionalized; Polysciences) to the solution (75 μl/ml). The solution was then sonicated and immediately vortexed in 500 μl of oil phase [HFE-7500 oil (3M) supplemented with 2 wt % of 008-FluoroSurfactant (RAN Biotech)] to form polydisperse droplets with an individual microcross inside, preventing the settlement and aggregation of microcrosses. The droplet-forming solution and oil phase were coinjected into the microfluidics via PE (polyethylene) tubing [inside diameter (ID), 1/32 inch; outer diameter (OD), 1/16 inch; Intramedic] and 20-gauge × 1/4 needles connected to 1 ml (for aqueous stream) and PE tubing (ID, 0.022 inch; OD, 0.042 inch; Intramedic) and 23-gauge × 1/4 needles connected to 5-ml (for oil stream) syringes. The syringes were mounted upright on the syringe pump (PHD 2000, Harvard Apparatus, Holliston, MA, USA), and the fluids were pumped with a flow rate of 50 μl/hour based on the 1-ml syringe. Cross-linker solution (120 μl) containing 15 wt % of PEG 8-NBA (MW = 20 kDa) was also infused into the device through picoinjection channel by PE tubing (ID, 1/32 inch; OD, 1/16 inch; Intramedic) connected to the pressurized solution at 280 mbar inside the 1.5-ml tube using the Fluigent LineUp Series pressure pump. After the system became stable, the high AC voltage (250 V at 1 kHz) was applied to the inlet and picoinjection electrodes, creating a high electric field to merge the polydisperse droplets into a continuous flow and to trigger the injection of the cross-linker, respectively. After the injection, the droplets were passed through a downstream serpentine structure for passive mixing to homogenously cross-link before the complete gelation at the collection chamber. The final microgels were then collected in a 5-ml centrifuge tube. After the collection of the microgels, the oil phase was aspirated off, and 20% (v/v) of PFO (1*H*,1*H*,2*H*,2*H*-perfluoro-1-octanol; 97%; MilliporeSigma) in Novec 7500 oil was added to break the emulsions. After the removal of oil/PFO phase, the droplets were washed three times with Novec 7500 oil, hexane (MilliporeSigma), and 0.1 wt % of Pluronic F-127 (MilliporeSigma), in that order. To collect the microrobot probes from the rest of the microgel, an Allen wrench was magnetized, submerged in the microgel solution, and transferred to 1 ml of deionized water, followed by demagnetization of the wrench and subsequent vortexing to allow the microrobot probes to be suspended in solution.

Materials characterization

The elemental composition of the electroplated Co-Pt was characterized with a scanning electron microscope equipped with energy-dispersive x-ray spectroscopy (EDS) (FEI NOVA 430) with the column voltage of 18 kV (*63*). EDS analysis showed a near

equiatomic composition of the electroplated microcross (51% Co and 49% Pt). A vibrating sample magnetometer (ADE Technologies Model EV9) capable of applying magnetic field up to 2.5 T was used to measure the magnetic properties of the Co-Pt film, including coercivity, remanence, and saturation magnetization. The film thickness was measured with a Keyence VK-X1000 3D laser scanning confocal microscope. Additional Materials and Methods are listed in the Supplementary Materials.

Statistical analysis

Two-tailed paired or unpaired Student's *t* test was performed for analyses.

Supplementary Materials

This PDF file includes:
Materials and Methods
Figs. S1 to S24
References (*72*–*74*)

Other Supplementary Material for this manuscript includes the following:
Movies S1 to S3
MDAR Reproducibility Checklist

REFERENCES AND NOTES

1. F. Chowdhury, B. Huang, N. Wang, Cytoskeletal prestress: The cellular hallmark in mechanobiology and mechanomedicine. *Cytoskeleton (Hoboken).* **78**, 249–276 (2021).
2. N. Wang, K. Naruse, D. Stamenović, J. J. Fredberg, S. M. Mijailovich, I. M. Tolić-Nørrelykke, T. Polte, R. Mannix, D. E. Ingber, Mechanical behavior in living cells consistent with the tensegrity model. *Proc. Natl. Acad. Sci. U.S.A.* **98**, 7765–7770 (2001).
3. N. Wang, I. M. Tolić-Nørrelykke, J. Chen, S. M. Mijailovich, J. P. Butler, J. J. Fredberg, D. Stamenović, Cell prestress. I. Stiffness and prestress are closely associated in adherent contractile cells. *Am. J. Physiol. Cell Physiol.* **282**, C606–C616 (2002).
4. V. F. Fiore, M. Krajnc, F. G. Quiroz, J. Levorse, H. A. Pasolli, S. Y. Shvartsman, E. Fuchs, Mechanics of a multilayer epithelium instruct tumour architecture and function. *Nature* **585**, 433–439 (2020).
5. R. M. Hochmuth, Micropipette aspiration of living cells. *J. Biomech.* **33**, 15–22 (2000).
6. J. Guck, R. Ananthakrishnan, H. Mahmood, T. J. Moon, C. C. Cunningham, J. Käs, The optical stretcher: A novel laser tool to micromanipulate cells. *Biophys. J.* **81**, 767–784 (2001).
7. J. C. Crocker, M. T. Valentine, E. R. Weeks, T. Gisler, P. D. Kaplan, A. G. Yodh, D. A. Weitz, Two-point microrheology of inhomogeneous soft materials. *Phys. Rev. Lett.* **85**, 888–891 (2000).
8. Y. Tseng, T. P. Kole, D. Wirtz, Micromechanical mapping of live cells by multiple-particle-tracking microrheology. *Biophys. J.* **83**, 3162–3176 (2002).
9. A. Ashkin, J. Dziedzic, Optical trapping and manipulation of viruses and bacteria. *Science* **235**, 1517–1520 (1987).
10. G. Binnig, C. F. Quate, C. Gerber, Atomic force microscope. *Phys. Rev. Lett.* **56**, 930–933 (1986).
11. N. Wang, J. Butler, D. Ingber, Mechanotransduction across the cell surface and through the cytoskeleton. *Science* **260**, 1124–1127 (1993).
12. B. Fabry, G. N. Maksym, S. A. Shore, P. E. Moore, R. A. Panettieri Jr., J. P. Butler, J. J. Fredberg, Selected contribution: Time course and heterogeneity of contractile responses in cultured human airway smooth muscle cells. *J. Appl. Physiol.* **91**, 986–994 (2001).
13. A. R. Bausch, F. Ziemann, A. A. Boulbitch, K. Jacobson, E. Sackmann, Local measurements of viscoelastic parameters of adherent cell surfaces by magnetic bead microrheometry. *Biophys. J.* **75**, 2038–2049 (1998).
14. S. Hu, L. Eberhard, J. Chen, J. C. Love, J. P. Butler, J. J. Fredberg, G. M. Whitesides, N. Wang, Mechanical anisotropy of adherent cells probed by a three-dimensional magnetic twisting device. *Am. J. Physiol. Cell Physiol.* **287**, C1184–C1191 (2004).
15. Y. Zhang, F. Wei, Y.-C. Poh, Q. Jia, J. Chen, J. Chen, J. Luo, W. Yao, W. Zhou, W. Huang, F. Yang, Y. Zhang, N. Wang, Interfacing 3D magnetic twisting cytometry with confocal fluorescence microscopy to image force responses in living cells. *Nat. Protoc.* **12**, 1437–1450 (2017).
16. F. Wei, X. Xu, C. Zhang, Y. Liao, B. Ji, N. Wang, Stress fiber anisotropy contributes to force-mode dependent chromatin stretching and gene upregulation in living cells. *Nat. Commun.* **11**, 4902 (2020).
17. P.-H. Wu, D. R.-B. Aroush, A. Asnacios, W.-C. Chen, M. E. Dokukin, B. L. Doss, D. Wirtz, A comparison of methods to assess cell mechanical properties. *Nat. Methods* **15**, 491–498 (2018).
18. F. Serwane, A. Mongera, P. Rowghanian, D. A. Kealhofer, A. A. Lucio, Z. M. Hockenbery, O. Campàs, In vivo quantification of spatially varying mechanical properties in developing tissues. *Nat. Methods* **14**, 181–186 (2017).
19. A. J. Thompson, E. K. Pillai, I. B. Dimov, S. K. Foster, C. E. Holt, K. Franze, Rapid changes in tissue mechanics regulate cell behaviour in the developing embryonic brain. *eLife* **8**, e39356 (2019).
20. M. Dembo, Y.-L. Wang, Stresses at the cell-to-substrate interface during locomotion of fibroblasts. *Biophys. J.* **76**, 2307–2316 (1999).
21. N. Q. Balaban, U. S. Schwarz, D. Riveline, P. Goichberg, G. Tzur, I. Sabanay, B. Geiger, Force and focal adhesion assembly: A close relationship studied using elastic micropatterned substrates. *Nat. Cell Biol.* **3**, 466–472 (2001).
22. J. P. Butler, I. M. Tolić-Nørrelykke, B. Fabry, J. J. Fredberg, Traction fields, moments, and strain energy that cells exert on their surroundings. *Am. J. Physiol. Cell Physiol.* **282**, C595–C605 (2002).
23. I. M. Tolić-Nørrelykke, J. P. Butler, J. Chen, N. Wang, Spatial and temporal traction response in human airway smooth muscle cells. *Am. J. Physiol. Cell Physiol.* **283**, C1254–C1266 (2002).
24. J. L. Tan, J. Tien, D. M. Pirone, D. S. Gray, K. Bhadriraju, C. S. Chen, Cells lying on a bed of microneedles: An approach to isolate mechanical force. *Proc. Natl. Acad. Sci. U.S.A.* **100**, 1484–1489 (2003).
25. J. P. Califano, C. A. Reinhart-King, Substrate stiffness and cell area predict cellular traction stresses in single cells and cells in contact. *Cell. Mol. Bioeng.* **3**, 68–75 (2010).
26. L. Trichet, J. Le Digabel, R. J. Hawkins, S. R. Vedula, M. Gupta, C. Ribrault, P. Hersen, R. Voituriez, B. Ladoux, Evidence of a large-scale mechanosensing mechanism for cellular adaptation to substrate stiffness. *Proc. Natl. Acad. Sci. U.S.A.* **109**, 6933–6938 (2012).
27. S. A. Maskarinec, C. Franck, D. A. Tirrell, G. Ravichandran, Quantifying cellular traction forces in three dimensions. *Proc. Natl. Acad. Sci. U.S.A.* **106**, 22108–22113 (2009).
28. W. R. Legant, J. S. Miller, B. L. Blakely, D. M. Cohen, G. M. Genin, C. S. Chen, Measurement of mechanical tractions exerted by cells in three-dimensional matrices. *Nat. Methods* **7**, 969–971 (2010).
29. J. C. del Álamo, R. Meili, B. Álvarez-González, B. Alonso-Latorre, E. Bastounis, R. Firtel, J. C. Lasheras, Three-dimensional quantification of cellular traction forces and mechano-sensing of thin substrata by fourier traction force microscopy. *PLOS ONE* **8**, e69850 (2013).
30. B. Álvarez-González, S. Zhang, M. Gómez-González, R. Meili, R. A. Firtel, J. C. Lasheras, J. C. Del Álamo, Two-layer elastographic 3-D traction force microscopy. *Sci. Rep.* **7**, 39315 (2017).
31. M. Cóndor, J. Steinwachs, C. Mark, J. M. García-Aznar, B. Fabry, Traction force microscopy in 3-dimensional extracellular matrix networks. *Curr. Protoc. Cell Biol.* **75**, 10.22.1–10.22.20 (2017).
32. D. Vorselen, Y. Wang, M. M. de Jesus, P. K. Shah, M. J. Footer, M. Huse, W. Cai, J. A. Theriot, Microparticle traction force microscopy reveals subcellular force exertion patterns in immune cell-target interactions. *Nat. Commun.* **11**, 20 (2020).
33. J. H. Kim, X. Serra-Picamal, D. T. Tambe, E. H. Zhou, C. Y. Park, M. Sadati, J. A. Park, R. Krishnan, B. Gweon, E. Millet, J. P. Butler, X. Trepat, J. J. Fredberg, Propulsion and navigation within the advancing monolayer sheet. *Nat. Mater.* **12**, 856–863 (2013).
34. R. Serrano, A. Aung, Y. T. Yeh, S. Varghese, J. C. Lasheras, J. C. Del Álamo, Three-dimensional monolayer stress microscopy. *Biophys. J.* **117**, 111–128 (2019).
35. N. Mandriota, C. Friedsam, J. A. Jones-Molina, K. V. Tatem, D. E. Ingber, O. Sahin, Cellular nanoscale stiffness patterns governed by intracellular forces. *Nat. Mater.* **18**, 1071–1077 (2019).
36. J. Zhou, S. Pal, S. Maiti, L. A. Davidson, Force production and mechanical accommodation during convergent extension. *Development* **142**, 692–701 (2015).
37. O. Campàs, T. Mammoto, S. Hasso, R. A. Sperling, D. O'Connell, A. G. Bischof, R. Maas, D. A. Weitz, L. Mahadevan, D. E. Ingber, Quantifying cell-generated mechanical forces within living embryonic tissues. *Nat. Methods* **11**, 183–189 (2014).
38. A. Mongera, P. Rowghanian, H. J. Gustafson, E. Shelton, D. A. Kealhofer, E. K. Carn, F. Serwane, A. A. Lucio, J. Giammona, O. Campàs, A fluid-to-solid jamming transition underlies vertebrate body axis elongation. *Nature* **561**, 401–405 (2018).
39. N. Träber, K. Uhlmann, S. Girardo, G. Kesavan, K. Wagner, J. Friedrichs, R. Goswami, K. Bai, M. Brand, C. Werner, D. Balzani, J. Guck, Polyacrylamide bead sensors for in vivo quantification of cell-scale stress in zebrafish development. *Sci. Rep.* **9**, 17031 (2019).
40. H. T. Nia, H. Liu, G. Seano, M. Datta, D. Jones, N. Rahbari, J. Incio, V. P. Chauhan, K. Jung, J. D. Martin, V. Askoxylakis, T. P. Padera, D. Fukumura, Y. Boucher, F. J. Hornicek, A. J. Grodzinsky, J. W. Baish, L. L. Munn, R. K. Jain, Solid stress and elastic energy as measures of tumour mechanopathology. *Nat. Biomed. Eng.* **1**, 0004 (2017).

41. A. Manduca, T. E. Oliphant, M. A. Dresner, J. L. Mahowald, S. A. Kruse, E. Amromin, J. P. Felmlee, J. F. Greenleaf, R. L. Ehman, Magnetic resonance elastography: Non-invasive mapping of tissue elasticity. *Med. Image Anal.* **5**, 237–254 (2001).
42. C. C. Park, P. Nguyen, C. Hernandez, R. Bettencourt, K. Ramirez, L. Fortney, J. Hooker, E. Sy, M. T. Savides, M. H. Alquiraish, M. A. Valasek, E. Rizo, L. Richards, D. Brenner, C. B. Sirlin, R. Loomba, Magnetic resonance elastography vs transient elastography in detection of fibrosis and noninvasive measurement of steatosis in patients with biopsy-proven nonalcoholic fatty liver disease. *Gastroenterology* **152**, 598–607.e2 (2017).
43. A. Qayyum, K. P. Hwang, J. Stafford, A. Verma, D. M. Maru, S. Sandesh, J. Sun, R. C. Pestana, R. Avritscher, M. M. Hassan, H. Amin, A. Rashid, I. I. Wistuba, R. L. Ehman, J. Ma, A. O. Kaseb, Immunotherapy response evaluation with magnetic resonance elastography (MRE) in advanced HCC. *J. Immunother. Cancer* **7**, 329 (2019).
44. E. Mohagheghian, J. Luo, J. Chen, G. Chaudhary, J. Chen, J. Sun, R. H. Ewoldt, N. Wang, Quantifying compressive forces between living cell layers and within tissues using elastic round microgels. *Nat. Commun.* **9**, 1878 (2018).
45. D. D. McKinnon, T. E. Brown, K. A. Kyburz, E. Kiyotake, K. S. Anseth, Design and characterization of a synthetically accessible, photodegradable hydrogel for user-directed formation of neural networks. *Biomacromolecules* **15**, 2808–2816 (2014).
46. S. Khetan, M. Guvendiren, W. R. Legant, D. M. Cohen, C. S. Chen, J. A. Burdick, Degradation-mediated cellular traction directs stem cell fate in covalently crosslinked three-dimensional hydrogels. *Nat. Mater.* **12**, 458–465 (2013).
47. C. Bonnet-Gonnet, L. Belloni, B. Cabane, Osmotic pressure of latex dispersions. *Langmuir* **10**, 4012–4021 (1994).
48. J. Cappello, V. d'Herbemont, A. Lindner, O. du Roure, Microfluidic in-situ measurement of Poisson's ratio of hydrogels. *Micromachines (Basel).* **11**, 318 (2020).
49. J. Liu, Y. Tan, H. Zhang, Y. Zhang, P. Xu, J. Chen, Y. C. Poh, K. Tang, N. Wang, B. Huang, Soft fibrin gels promote selection and growth of tumorigenic cells. *Nat. Mater.* **11**, 734–741 (2012).
50. Y. Liu, J. Lv, X. Liang, X. Yin, L. Zhang, D. Chen, X. Jin, R. Fiskesund, K. Tang, J. Ma, H. Zhang, W. Dong, S. Mo, T. Zhang, F. Cheng, Y. Zhou, J. Xie, N. Wang, B. Huang, Fibrin stiffness mediates dormancy of tumor-repopulating cells via a Cdc42-driven Tet2 epigenetic program. *Cancer Res.* **78**, 3926–3937 (2018).
51. M. Yang, T. Rito, J. Metzger, J. Naftaly, R. Soman, J. Hu, D. F. Albertini, D. H. Barad, A. H. Brivanlou, N. Gleicher, Depletion of aneuploid cells in human embryos and gastruloids. *Nat. Cell Biol.* **23**, 314–321 (2021).
52. M. E. Dolega, M. Delarue, F. Ingremeau, J. Prost, A. Delon, G. Cappello, Cell-like pressure sensors reveal increase of mechanical stress towards the core of multicellular spheroids under compression. *Nat. Commun.* **8**, 14056 (2017).
53. C. Yang, M. W. Tibbitt, L. Basta, K. S. Anseth, Mechanical memory and dosing influence stem cell fate. *Nat. Mater.* **13**, 645–652 (2014).
54. A. J. Engler, S. Sen, H. L. Sweeney, D. E. Discher, Matrix elasticity directs stem cell lineage specification. *Cell* **126**, 677–689 (2006).
55. J. Rheinlaender, H. Wirbel, T. E. Schäffer, Spatial correlation of cell stiffness and traction forces in cancer cells measured with combined SICM and TFM. *RSC Adv.* **11**, 13951–13956 (2021).
56. M. G. Ondeck, A. Kumar, J. K. Placone, C. M. Plunkett, B. F. Matte, K. C. Wong, L. Fattet, J. Yang, A. J. Engler, Dynamically stiffened matrix promotes malignant transformation of mammary epithelial cells via collective mechanical signaling. *Proc. Natl. Acad. Sci. U.S.A.* **116**, 3502–3507 (2019).
57. L. Sikic, E. Schulman, A. Kosklin, A. Saraswathibhatla, O. Chaudhuri, J. Pokki, Nanoscale tracking combined with cell-scale microrheology reveals stepwise increases in force generated by cancer cell protrusions. *Nano Lett.* **22**, 7742–7750 (2022).
58. S. E. Webb, A. L. Miller, Calcium signalling during embryonic development. *Nat. Rev. Mol. Cell Biol.* **4**, 539–551 (2003).
59. M. Duch, N. Torras, M. Asami, T. Suzuki, M. I. Arjona, R. Gómez-Martínez, M. D. VerMilyea, R. Castilla, J. A. Plaza, A. C. F. Perry, Tracking intracellular forces and mechanical property changes in mouse one-cell embryo development. *Nat. Mater.* **19**, 1114–1123 (2020).
60. S. Shamipour, R. Kardos, S. L. Xue, B. Hof, E. Hannezo, C. P. Heisenberg, Bulk actin dynamics drive phase segregation in zebrafish oocytes. *Cell* **177**, 1463–1479.e18 (2019).
61. J. G. Dumortier, M. Le Verge-Serandour, A. F. Tortorelli, A. Mielke, L. de Plater, H. Turlier, J. L. Maître, Hydraulic fracturing and active coarsening position the lumen of the mouse blastocyst. *Science* **365**, 465–468 (2019).
62. K. Leonavicius, C. Royer, C. Preece, B. Davies, J. S. Biggins, S. Srinivas, Mechanics of mouse blastocyst hatching revealed by a hydrogel-based microdeformation assay. *Proc. Natl. Acad. Sci. U.S.A.* **115**, 10375–10380 (2018).
63. E. Priel, T. Priel, I. Szaingurten-Solodkin, T. Wainstock, Y. Perets, A. Zeadna, A. Harlev, E. Lunenfeld, E. Levitas, I. Har-Vardi, Zona pellucida shear modulus, a possible novel non-invasive method to assist in embryo selection during in-vitro fertilization treatment. *Sci. Rep.* **10**, 14066 (2020).
64. J. L. Maître, H. Turlier, R. Illukkumbura, B. Eismann, R. Niwayama, F. Nédélec, T. Hiiragi, Asymmetric division of contractile domains couples cell positioning and fate specification. *Nature* **536**, 344–348 (2016).
65. J. L. Maître, R. Niwayama, H. Turlier, F. Nédélec, T. Hiiragi, Pulsatile cell-autonomous contractility drives compaction in the mouse embryo. *Nat. Cell Biol.* **17**, 849–855 (2015).
66. Y. Kim, E. Genevriere, P. Harker, J. Choe, M. Balicki, R. W. Regenhardt, J. E. Vranic, A. A. Dmytriw, A. B. Patel, X. Zhao, Telerobotic neurovascular interventions with magnetic manipulation. *Sci. Robot.* **7**, eabg9907 (2022).
67. G. Amadei, C. E. Handford, C. Qiu, J. De Jonghe, H. Greenfeld, M. Tran, B. K. Martin, D. Y. Chen, A. Aguilera-Castrejon, J. H. Hanna, M. B. Elowitz, F. Hollfelder, J. Shendure, D. M. Glover, M. Zernicka-Goetz, Embryo model completes gastrulation to neurulation and organogenesis. *Nature* **610**, 143–153 (2022).
68. A. Aguilera-Castrejon, B. Oldak, T. Shani, N. Ghanem, C. Itzkovich, S. Slomovich, S. Tarazi, J. Bayerl, V. Chugaeva, M. Ayyash, S. Ashouokhi, D. Sheban, N. Livnat, L. Lasman, S. Viukov, M. Zerbib, Y. Addadi, Y. Rais, S. Cheng, Y. Stelzer, H. Keren-Shaul, R. Shlomo, R. Massarwa, N. Novershtern, I. Maza, J. H. Hanna, Ex utero mouse embryogenesis from pre-gastrulation to late organogenesis. *Nature* **593**, 119–124 (2021).
69. O. D. Oniku, B. Qi, D. P. Arnold, Electroplated thick-film cobalt platinum permanent magnets. *J. Magnetism Magnetic Mater.* **416**, 417–428 (2016).
70. S. Moise, E. Céspedes, D. Soukup, J. M. Byrne, A. J. El Haj, N. D. Telling, The cellular magnetic response and biocompatibility of biogenic zinc- and cobalt-doped magnetite nanoparticles. *Sci. Rep.* **7**, 39922 (2017).
71. J. F. Fowler Jr., J. H. Perryman, B. Quinlan, Positive patch-test reactions to platinum are rare. *Dermatitis* **19**, 146–147 (2008).
72. D. Turner, P. Crozier, P. Reu, Digital Image Correlation Engine. Computer software, version 00. 6 October 2015;https://osti.gov//servlets/purl/1245432.
73. J. R. Tse, A. J. Engler, Preparation of hydrogel substrates with tunable mechanical properties. *Curr. Protoc. Cell Biol.* **47**, 10.16.1–10.16.16 (2010).
74. E. Bar-Kochba, J. Toyjanova, E. Andrews, K.-S. Kim, C. A. Franck, A fast iterative digital volume correlation algorithm for large deformations. *Exp. Mech.* **55**, 261–274 (2015).

Acknowledgments: We thank G. A. Mensing and J. Maduzia at the Micro-Nano-Mechanical Systems Cleanroom Laboratory of Department of Mechanical Science and Engineering at UIUC for technical assistance. **Funding:** This study was funded by the National Institutes of Health grants R01 GM072744 (to N.W.), F31 DK126427 (to F.M.Y.), and R01 DK120921 (to K.S.A.); National Science Foundation (NSF 2033723) (to K.S.A.); National Natural Science Foundation of China (11902121 and 32071306) (to J.C.); Program for Huazhong University of Science and Technology Academic Frontier Youth Team (2018QYTD01) (to J.C.); and the Leonard C. and Mary Lou Hoeft Endowed Professorship in Engineering at UIUC (to N.W.). **Author contributions:** Conceptualization: N.W. Methodology: N.W., E.M., J.L., F.M.Y., F.W., P.B., and K.A. Investigation: E.M., J.L., F.M.Y., F.W., P.B., K.A., F.R., Y.W., X.L., and C.J. Funding acquisition: N.W., F.M.Y., K.S.A., and J.C. Project administration: N.W. Supervision: N.W. Writing—original draft: N.W., E.M., J.L., F.M.Y., and F.W. Writing—review and editing: N.W., Z.L., J.C., D.P.A., and K.S.A. **Competing interests:** The authors declare that they have no competing interests. **Data and materials availability:** All data needed to evaluate the findings are present in the paper and/or the Supplementary Materials. The codes for traction force calculations can be retrieved from https://github.com/pvbhala/3D-traction force-MATLAB-code.

Submitted 12 May 2022
Resubmitted 28 May 2022
Accepted 22 December 2022
Published 25 January 2023
10.1126/scirobotics.adc9800

Science Robotics

Quantifying stiffness and forces of tumor colonies and embryos using a magnetic microrobot

Erfan Mohagheghian, Junyu Luo, F. Max Yavitt, Fuxiang Wei, Parth Bhala, Kshitij Amar, Fazlur Rashid, Yuzheng Wang, Xingchen Liu, Chenyang Ji, Junwei Chen, David P. Arnold, Zhen Liu, Kristi S. Anseth, and Ning Wang

Sci. Robot. **8** (74), eadc9800. DOI: 10.1126/scirobotics.adc9800

Science Robotics (ISSN 2470-9476) is published by the American Association for the Advancement of Science. 1200 New York Avenue NW, Washington, DC 20005. The title *Science Robotics* is a registered trademark of AAAS.